Co-gasification of digestate and lignite in a downdraft fixed bed gasifier: Effect of temperature

Shengqiang Chang [a,b], Zhikai Zhang [a], Lixia Cao [a], Liqiang Ma [b], Siming You [c,*], Wangliang Li [a,*]

a. The Key Laboratory of Green Process and Engineering, Institute of Process Engineering, Chinese Academy of Sciences, 1 Zhongguancun, Haidian District, Beijing 100190, China

b. School of Chemical & Environmental Engineering, China University of Mining & Technology (Beijing), Beijing 100083, China

c. Division of Systems, Power and Energy, James Watt School of Engineering, University of Glasgow, UK, G12 8QQ

*Corresponding author: wlli@ipe.ac.cn (Wangliang Li); siming.you@glasgow.ac.uk (Siming You)

Abstract: To improve energy efficiency and biomass utilization in the process of anaerobic digestion, co-gasification is considered as an effective method to post-treat anaerobic digestion residues. In this work, the effect of temperature (650 °C, 750 °C, 850 °C and 950 °C) on the co-gasification of digestate and lignite was thoroughly investigated in a downdraft fixed bed gasifier. The results showed that the increase of gasification temperature increased the gas yield and the lower heating value (LHV) of product gas. Physicochemical properties of biochar were characterized by physical adsorption analyzer, Fourier transform infrared spectroscopy (FT-IR), Raman spectroscopy and thermogravimetric analyzer (TG). It was shown that the average pore diameter increased in the range of 650 °C to 950 °C, while specific surface area and pore volume first increased from 650 °C to 850 °C and then decreased at 950 °C. The Raman analysis of biochar indicated that small aromatic rings condensed to large aromatic ring and increased the content of $C_{aromatic}$-C_{alkyl} and the crosslinking density at higher temperature. The variation of biochar properties at the higher temperature caused a decrease in the gasification reactivity. With the increase of temperature, the content of carbolic oil in the tar increased, but the contents of light oil, naphthalene oil and washing oil decreased. This study comprehensively analyzed the product properties and demonstrated the feasibility of co-gasification of digestate and lignite.

Keywords: co-gasification; lignite; digestate; downdraft fixed bed gasifier; biochar

Nomenclature

Symbols

a	Slope of fitting straight line	Q	Quantity adsorbed [mL·g^{-1}]
c	Calculated by difference [%]	$R_{0.9}$	Reactivity index [min^{-1}]
C	Constant	R^2	Correlation coefficient
C_{CO_2}	CO_2 concentration in the gas [vol.%]	T	Temperature [°C]
M	Total mass of feedstock at each run [kg]	$t_{0.9}$	Gasification time when the conversion of biochar reaches to 0.9 [min]
G, D, S, G_R, V_L, V_R	Peak names of Raman spectroscopy	V_{gas}	Volume of CO, CO_2, H_2, CH_4 and C_nH_m [Nm^3]
I_D, I_G, I_{GR}, I_{VL}, I_{VR}, I_S	Peak area	x_n	Molarity of all gases (n=1,2···7)
P/P_0	Relative pressure of equilibrium and saturation	α	Content of impurity in CO_2 cylinder [%]
P_0/P	Relative pressure of saturation and equilibrium		

Abbreviations

ad	Air dry	GC-MS	Gas chromatography-mass spectrometer analyzer
AD	Anaerobic digestion	HSAD	High-solid anaerobic digestion
apd	Average pore dimeter [nm]	i.e.	Id est
a.u.	Arbitrary unit	IUPAC	International union of pure and applied chemistry
BET	Brunauer–Emmett–Teller	LHV	Lower heating value
C=C	Carbonyl	N	Nitrogen (monoatomic)
$C_{aromatic}$-C_{alkyl}	Carbon-carbon bond between aromatic and alkyl	Nm^3	Refers to m^3 at normal pressure (1.013×10^5 Pa) and temperature (0 °C)
C-H	Carbon-hydrogen bond	NO_x	Nitrogen oxide
CH_2	Methylene	O	Oxygen (monoatomic)
CH_4	Methane	P_2O_5	Phosphorus pentoxide
CHx	Alkyl	S	Sulfur (monoatomic)
C_nH_m	Hydrocarbon compounds	SO_x	Sulfur-oxygen species
Eq.	Equation	STP	Standard temperature and pressure
FD	Fractal dimension	TCD	Thermal conductivity detector
FHH	Frenkel–Halsey–Hill	TG	Thermogravimetric Analyzer
F.S	Full scale	vol.%	Volume percentage [%]
FT-IR	Fourier transform infrared spectroscopy	wt.%	Weight percentage [%]
GC	Gas chromatography		

1. Introduction

Because of the increasing energy consumption, depleting fossil fuel reserves, and worsening environment related to the excessive use of fossil fuels, alternative sources of renewable energies is receiving increasing attention [1]. The present concentration of carbon dioxide (CO_2) in the atmosphere exceeds 400 ppm and is proposed to reach 530 ppm and 650 ppm in 2050 and 2100, which will increase the global average temperature by 2.0 °C - 5.6 °C [2].

High-solid anaerobic digestion (HSAD) is an effective method to battle the global warming by recovering energy from organic biomass [3]. However, the disposal of a by-product of HSAD, digestate, is challenging from the perspective of environment safety [4]. Digestate is a mixture of undigested biomass, sludge and manure from an anaerobic digestion (AD) system. In recent years, the development of biogas industry has caught the attention of the Chinese government. By the end of 2015, there were 110,975 biogas plants and 41.93 million household biogas digesters in China. The output of digestate increased significantly and rapidly, mainly used as soil fertilizer [5]. But the digestate is rich in hazardous materials, for instance, heavy metals, fungicides, pathogens, nitrogen compounds and trace herbicides, which may have latent hazards on human being, animals and crops [6]. The landfilling of digestate may lead to environmental pollution, land occupancy and greenhouse gas emissions. Accordingly, the resource reutilization of digestate becomes an urgent problem to be solved.

In the AD process, only part of the cellulose and hemicellulose has been hydrolyzed because of the rigid structure and resistance of non-biodegradable lignin, leading to a low energy conversion efficiency of approximately 33-50 % [7, 8]. In the digestate, there are still many useful ingredients such as lignin. As biowaste, the digestate would be one promising alternate source to generate sustainable energy. In China, the projects where the digestate mixes with other combustibles from waste to produce heat and power have been listed in the National Key Energy-Saving Low-Carbon Technology Promotion Catalogue (2017 Version, Low Carbon Section). Once this kind of technology is massively industrialized, the annual emission reduction of CO_2 is expected to reach 1.85 million tons [9].

Gasification is a thermochemical technology that could convert the feedstock into the flammable gas (i.e. synthesis gas) effectively [10-12]. Chen et al. [7] conducted the air gasification of digestate in a downdraft fixed bed gasifier, and the results showed that the optimal lower heating value of product gas was 4.78 $MJ \cdot Nm^{-3}$. Yao et al. [13] proposed the co-gasification of woody chips and digestate, and the optimal energy efficiency was 70.8 % when the mass ratio of woody chips was 80 wt.% and the moisture content of digestate was 30 wt.%. Although the gasification of digestate can reduce the volume of waste to be landfilled, kill the germs and immobilize the toxic metals in the inorganic matrix [14], it is facing several

challenges, such as low caloric value gas and low gasification efficiency, preventing the wide application of the technology.

Over the past decades, the low energy efficiency and significant air pollution of coal combustion limited its application for heat and energy production [15]. Predictably, the coal will continue to be the main energy source despite the fact that the China's energy structure is changing for the next several years [16, 17]. Seeking efficient and clean utilization of coal appears to be one of the main research focuses. The co-gasification of biomass and coal has been widely investigated owing to its high energy conversion efficiency, remarkable economy benefits and operational stability. The co-gasification of biomass and coal can suppress the generation of SO_x and NO_x and cut the greenhouse gas emission [14, 18, 19]. Besides, the addition of coal in the mixture will make up the seasonal supply of biomass (e.g. digestate). Thengane et al. [20] used air as the gasification agent in the downdraft gasifier to deal with the garden waste pellets and coal. The LHV of gas reached to 3.05 $MJ \cdot Nm^{-3}$ at biomass ratio 75 wt.%. Wu et al. [21] added 50 wt.% coal into wheat straw, and the highest LHV of combustible gas achieved 14.21 $MJ \cdot Nm^{-3}$ in entrained flow bed with the preheating of gasification agent, which suggested that feeding the gasifier a combination of different fuels have synergy between their products and intermediates. Meanwhile, the co-gasification of different fuels will lead to maximize the performance, to reduce the carbon losses and to increase the energy content of syngas. However, the co-gasification of digestate and lignite has been rarely studied while it has the potential to bridge AD and gasification for high-efficient hybrid system development [22].

The co-gasification characteristics of biomass and coal is closely related to the reactor type and the operational conditions, such as temperature, gasification agent, mass ratios, etc [23]. Among them, the gasification temperature remarkably affected the release of volatiles from raw material and the gasification behaviors between the gasification agent and biochar. Cortazar et al. [24] found that the gasification temperature played a positive role in the improvement of gas yield and the tar removal. Meanwhile, comparing with other gasifiers, the fixed bed would be more easily controlled and more suitable to the co-gasification of biomass and coal. The fixed bed can promote the intimate contact between raw material particles and provide sufficient residence time. In terms of the downdraft fixed bed, the reduction zone is

where the gasification occurs. The coal can provide more stable reaction temperature for the co-gasification in the reduction zone. Moreover, the relatively slow thermal conversion process may enhance the tar cracking [25]. Collot et al. [26] studied the effect of reactor types on the co-gasification of biomass and coal finding that the tar cracking occurred in the fixed bed. Li et al. [22] studied the effects of mixing methods and the kinetics of the co-gasification of digestate and lignite, stating that the synergistic interaction was the most remarkable when the anaerobic digestion treatment time of biomass was 40 days. However, the effect of temperature on the co-gasification behavior of digestate and lignite was seldom reported.

Therefore, the main objective of this study was to study the effect of temperature (650 °C, 750 °C, 850 °C and 950 °C) on the co-gasification behavior of digestate and lignite by analyzing co-gasification products comprehensively.

2. Materials and methods

2.1. Materials

The digestate was collected from the high solid anaerobic digestion of corn straw, sludge and cattle manure. The coal was selected from the Xiaolongtan lignite. Prior to the experiments, the samples were dried at 105 ºC until constant weight and pulverized to below 150 mesh in a grinder. The ultimate analysis and proximate analysis of lignite and digestate have been published in our previous study, as shown in Table 1 [22].

Table 1 Ultimate analysis and proximate analysis of lignite and digestate [22].

	Ultimate analysis（wt%, ad）					Proximate analysis（wt%, d）		
	C	H	N	S	O[c]	Volatile matter	Ash	Fixed carbon
Lignite	52.04	4.66	1.48	1.31	25.92	54.01	12.09	33.89
Digestate	29.64	3.61	2.38	0.54	20.31	47.75	41.48	10.77

[c]: Calculated by difference.

2.2 Gasification experiment set-up

The experiments were conducted in a lab-scale downdraft fixed bed gasifier. Fig. 1 is the main process flow chart of digestate and lignite co-gasification in CO_2 [22]. The lab-scale downdraft fixed bed gasifier system contains a carrier gas system, electric heating furnaces, a downdraft reactor and gas detection system. The downdraft reactor contains a quartz tube, electric heating furnace and thermocouples. Wrapped by the electric heating furnace, the quartz tube is 600 mm high and has an internal diameter of 35 mm. In the middle of the quartz tube, there is a distributor plate where the

feedstock stored in the crucible is gasified in CO_2.

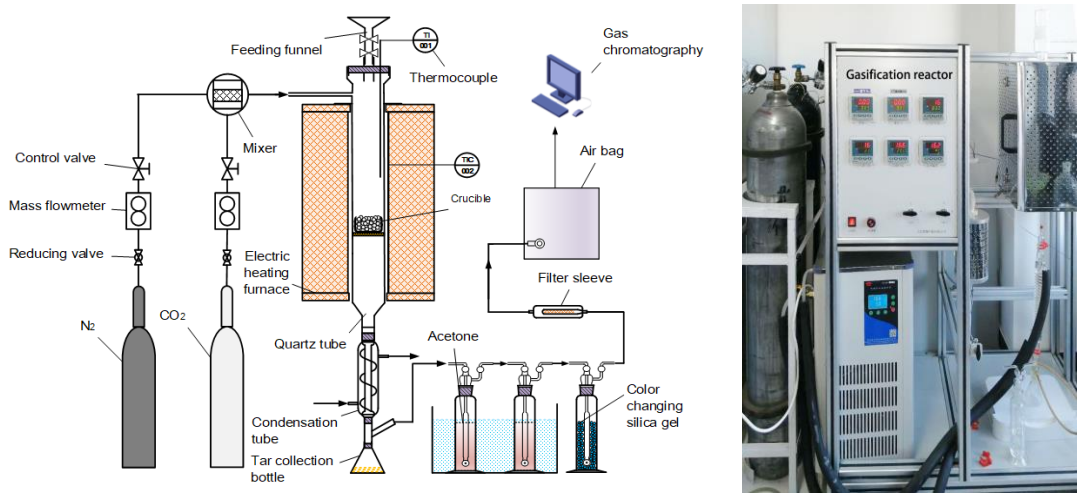

(a) (b)

Fig. 1. (a) Flow chart of the gasification system, (b) real picture of the system, for the co-gasification of digestate and lignite.

The digestate and the lignite were manually mixed with the mass ratio 1:1 by mortar for complete blending. For each run, 2.00±0.01 g of feedstock was loaded into the crucible in the gasifier. Before starting up, pure CO_2 (99.99 %) was preloaded at a flow rate of 1000 mL·min^{-1} for 10 min. Then, the flow rate of pure CO_2 was switched to 60 mL·min^{-1}. The gas flowmeter produced from Beijing Sevenstar Electronics Co.,Ltd., was used to control the CO_2 gas flow. The scope of the flowmeter ranges from 0 L·min^{-1} to 2.0 L·min^{-1}. The repeatability accuracy of the selected flowmeter is ±0.2 % F.S, namely ±4 mL error. Maximum working pressure is 1.0 MPa. Before each run, the CO_2 gas flow rate was calibrated by the soap-membrane flowmeter to guarantee that the CO_2 gas flowmeter properly operated. The downdraft gasifier was heated from the room temperature to the target temperature at a heating rate of 50 ºC·min^{-1}, and then, the temperature remained constant. The K-type thermocouple was selected to measure the temperature in the reactor and electric heating furnace in the range of 0 °C to 1300 °C. The maximum allowable error was ±0.4 % of the measured temperature (375 °C-1000 °C). The gas from the reactor passed through the vertical condensation tube, the ice-baths of acetone, silica gel and the filter to remove the tar, water and small particle impurities. The tar-free dry gas was collected in a gas bag and analyzed with gas chromatography to detect the proportion of each component. In this study, the gasification process proceeded for 46 min. The total reaction time in

reactor was identical and the properties of gasification products collected at the same time can be compared meaningfully. Then pure CO_2 was switched to pure N_2 (99.99 %) at a flow rate of 1000 mL·min^{-1} until the temperature in the gasifier dropped to room temperature. The reaction temperatures were chosen as 650 ºC, 750 ºC, 850 ºC and 950 ºC, respectively. The experiment was repeated three times for each run.

2.3. Analytical methods

The gas chromatography (Inficon, Micro GC 3000) was equipped with thermal conductivity detector (TCD) to analyze the product gas by external standard method. Back flushing was used as the method of injection gas. The injector temperature and transfer line temperature were 90 °C. The first chromatographic column was 5A molecular sieve and the column temperature was 80 °C, which was used to detect the H_2, CO and CH_4. Pure argon (99.999 %) was selected as carrier gas. The second chromatographic column was Plot Q and the column temperature was 60 °C, which was used to detect the hydrocarbons gas (C_nH_m, $n < 4$). The third chromatographic column was Plot U and the column temperature was 80 °C, which was used to detect the CO_2. Pure helium (99.999 %) was used as carrier gas of the subsequent two chromatographic columns. The dry gas LHV (MJ·Nm^{-3}) and CO_2 conversion was defined as follows [27, 28]:

$$LHV=(CO\times12600+H_2\times10794+CH_4\times35868+C_nH_m\times63546)/10^5 \quad (1)$$

where CO, H_2, CH_4, C_nH_m are the concentrations of the product gas, vol.%.

$$CO_2\ conversion=100\times(100-\alpha-C_{CO_2})/(100-\alpha)/(100+C_{CO_2}) \quad (2)$$

Where α is the content of impurity in CO_2 cylinder, 0.01 %, C_{CO_2} is the CO_2 concentration in the gas, vol.%.

The yield of product gas (Nm^3·kg^{-1}) was defined as follows [13, 22, 29]:

$$Yield=V_{gas}/M \quad (3)$$

where V_{gas} is the volume of CO, CO_2, H_2, CH_4 and C_nH_m, Nm^3, M is the total mass of feedstock at each run, kg.

Nitrogen adsorption experiments (temperature, 77 K) were carried out to characterize the biochar collected under different temperatures with a physical adsorption analyzer (Micromeritics, ASAP 2020HD88, America). Before the nitrogen adsorption experiments, all the biochar samples were degassed for 8 h at 200 °C under

vacuum. The surface area and average pore diameter (apd) of biochar samples were measured using BET (Brunauer–Emmett–Teller). The pore volume was calculated from the single point desorption total pore volume of pores. The organ functional groups of biochar samples were identified by Fourier transform infrared spectroscopy (FT-IR, Bruker, T27, Germany) at wave lengths ranging from 400 cm^{-1} to 4000 cm^{-1}. Each sample was scanned 32 times, with a resolution of 4 cm^{-1}. Prior to analysis, per 1 mg samples were mixed with per 100 mg KBr powder. The sample-powder mixture was reground by mortar and pestle homogeneously. Pellets were created using 70–80 mg of powder in a pellet press at 10 MPa of pressure. Besides, the evolution of carbon structure was characterized by the Raman spectrum (Horiba Scientific, LabRAM HP Evolution, Janpan). The Raman spectra from 1800 cm^{-1} to 800 cm^{-1} were analyzed through peak fitting using Origin software (version 9.0) with nine Gaussian bands combining the work of Li et al. [30] and the actual conditions in this article. The gasification reactivity of the biochar was investigated by a thermogravimetric analyzer (Setaram Labsys Evo, Lyon, Rhône Province, France) in CO_2 adopting the non-isothermal route. About 5.0 ± 0.2 mg biochar was put into the crucible. The reaction temperature was risen from room temperature to 950 ºC at 15 ºC·min^{-1} and kept the constant temperature for 30 min. The gasification reactivity of biochar was quantitated by the reactivity index ($R_{0.9}$) as follows [31]:

$$R_{0.9}=0.9/t_{0.9} \quad (4)$$

where $t_{0.9}$ is the gasification time when the conversion of biochar reaches to 0.9.

The fractal theory was used to characterize the unformed materials. The degree of surface irregularity can be quantified by the surface fractal dimension (FD) which ranges from 2 to 3 [32]. Based on the fractal version of the Frenkel–Halsey–Hill (FHH) equation of multilayer adsorption, the values of surface fractal dimension can be calculated through the single nitrogen adsorption isotherm [33, 34].

$$\ln Q=a\cdot\ln(\ln(P_0/P))+C \quad (5)$$

where Q is the quantity adsorbed, P_0/P is the relative pressure of saturation and equilibrium, C is a constant. Suppose Y is ln$Q$ and Y=ax+b. The parameter a is the slope of fitting straight line. The surface fractal dimension of biochar is determined by the coefficient a as follows:

$$FD=3+a \quad (6)$$

The analysis of the tar collected in the condensation system was carried out by a

gas chromatography-mass spectrometer analyzer (GC-MS, QP 2010 Ultra, Shimadzu, Japan). Helium (99.999 %) was used as carrier gas in gas chromatography module and carrier gas flow rate was 1.2 $mL \cdot min^{-1}$. Split ratio was 49:1. The chromatographic column was 30 m RTX-5MS quartz capillary column. The inner diameter was 0.25 mm and film thickness was 0.25 μm. The temperature of ion source was 200 ℃ and the scan range of mass to charge ratio was from 20 to 900 amu. Additionally, the tar was fractionated by a simulated distillation instrumentation (Agilent 7890A, America) according to the ASTM-D2887-01a standard. The column was stainless steel. The diameter of column was 0.53 mm and the length was 10 m, which was designed by Sinopec Research Institute of Petroleum Processing in China.

2.4. Reactions during gasification in CO_2 atmosphere

The thermal conversion behavior and the possible reactions of digestate and lignite under the CO_2 atmosphere in the fixed bed reactor are shown as follows. Eq. (7) shows the overall gasification reaction of digestate and lignite in the CO_2 atmosphere. The Boudouard reaction is presented in Eq. (8). The solid biochar gasification reactions processes are shown in Eq. (9) and Eq. (10). The homogeneous volatile reactions which are the piece of secondary reactions changing the evolved volatiles compositions are shown in Eq. (11) and Eq. (12) is the water–gas shift reaction. The tar gasification reactions and the tar cracking are presented in Eq. (13) and Eq. (14), respectively [35, 36]. The tar contained hundreds of chemical compounds, such as aromatic compounds with single to five rings, polycyclic aromatic hydrocarbons (PAHs), and some oxygen-containing hydrocarbons. The chemical formula cannot represent the characterization of tar completely. Therefore, tar was used in the formula (7), (13) and (14) directly.

$$\text{Digestate+Lignite+}x_1\text{CO}_2 \rightarrow x_2\text{H}_2+x_3\text{CO}+x_4\text{CO}_2+x_5\text{CH}_4+x_6\text{C}_n\text{H}_m+x_7\text{H}_2\text{O}+\text{Char+Tar} \quad \Delta H>0 \quad (7)$$

where x_1, x_2, x_3, x_4, x_5, x_6 *and* x_7 is the molarity of all gases.

$$\text{C} + \text{CO}_2 \leftrightarrow 2\text{CO} \quad \Delta H = +172\ kJ \cdot mol^{-1} \quad (8)$$

$$\text{C} + 2\text{H}_2 \rightarrow \text{CH}_4 \quad \Delta H = -75\ kJ \cdot mol^{-1} \quad (9)$$

$$\text{C} + \text{H}_2\text{O} \rightarrow \text{CO} + \text{H}_2 \quad \Delta H = +131\ kJ \cdot mol^{-1} \quad (10)$$

$$\text{CO} + 3\text{H}_2 \leftrightarrow \text{CH}_4 + \text{H}_2\text{O} \quad \Delta H = -206\ kJ \cdot mol^{-1} \quad (11)$$

257 $CO + H_2O \leftrightarrow CO_2 + H_2$ $\Delta H = -41\ kJ \cdot mol^{-1}$ (12)

258 $Tar + CO_2 \rightarrow CO + H_2$ $\Delta H = +980 \sim +3112\ kJ \cdot mol^{-1}$ (13)

259 $Tar \rightarrow CH_4 + H_2 + H_2O + C_nH_m$ $\Delta H > 0$ (14)

260 ## 3. Results and discussion

261 *3.1. Gas composition*

262 The effect of reaction temperature on gas composition was conducted at 650 °C,
263 750 °C, 850 °C and 950 °C with the mass ratio 1:1. As shown in Fig. 2a, the
264 temperature played a crucial role in the CO_2 gasification performance and had a
265 significant influence on the gas composition. The main components of the gas were CO
266 and CO_2. H_2, CH_4 and hydrocarbon compounds (C_nH_m) were also observed. With the
267 increase of gasification temperature, the CO content and the CO_2 conversion increased
268 obviously, due to the thermodynamic equilibrium enhancement of Eqs. (8) and (13). It
269 was also related to equilibrium of the water-gas shift reaction as shown in Eq. (12).

270 The content of C_nH_m was very low. Therefore, the content of CH_4 was similar to
271 the total content of C_nH_m. In Fig. 2, the red curve of CH_4 was overlapped with cyan
272 curve of C_nH_m. Meanwhile, the content of CH_4 decreased slightly with the increase of
273 temperature. The main reason for the decrease of CH_4 content in the product gas is the
274 increasing proportion of gasification gas and the decreasing proportion of pyrolysis gas.
275 Another reason was attributed to the thermal decomposition of methane at the
276 temperature of 700 °C [37].

277 $CH_4 \rightarrow C + 2H_2$ $\Delta H = +74.8\ kJ \cdot mol^{-1}$ (15)

278 In Fig. 2b, the gas yield increased with the increase of gasification temperature.
279 On the one hand, the tar as the primary gasification product was further cracked into gas
280 at the higher temperature. Besides, the lignite was featured with the high ratios of
281 heavy aromatic to aliphatic, highly ordered carbon fraction and high fixed carbon
282 content [38]. The increase of temperature can activate the carbon atom and break the
283 carbon chain in the aromatic ring rapidly, reacting with gasification agent-CO_2 to
284 produce gas. Thirdly, in the co-gasification process of digestate and lignite at CO_2
285 atmosphere, the reduction of CO_2 is an endothermic reaction. The increase of
286 temperature was beneficial to the shift of reaction equilibrium towards the products.
287 However, the CO_2 yield increased firstly and then decreased gradually, which was due
288 to the fact that the increase of temperature promoted the reaction-Eq. (7) and more CO_2

was consumed in the gasification reaction-Eq. (8). When the consumption rate of CO_2 was faster than the generation rate, the CO_2 yield declined. The LHV of gas increased with the increase of temperature. The CO content and CO_2 conversion followed the same trend. When the temperature was 950 °C, the LHV of gas was the highest, 6.52 $MJ \cdot Nm^{-3}$, and nearly twice that of the 650 °C.

The gasification performances can be significantly influenced by the metal contents such as Na, K, Ca, Fe, etc. The rate of catalytic gasification significantly increased in the presence of alkali and alkaline earth metals and transition metals in the char. The CO_2 co-gasification performances showed its great potentials in enhancing the gasification reactivity, mitigating the problem of agglomeration and alleviating the greenhouse effect, through the utilization of ash from biomass wastes as catalyst [39, 40]. As shown in our previous study, the lignite and digestate all contained many alkali metals and alkaline earth metals [22]. It is reasonable to believe that the alkali metals and alkaline earth metals in the ash played an important role in co-gasification of lignite and digestate.

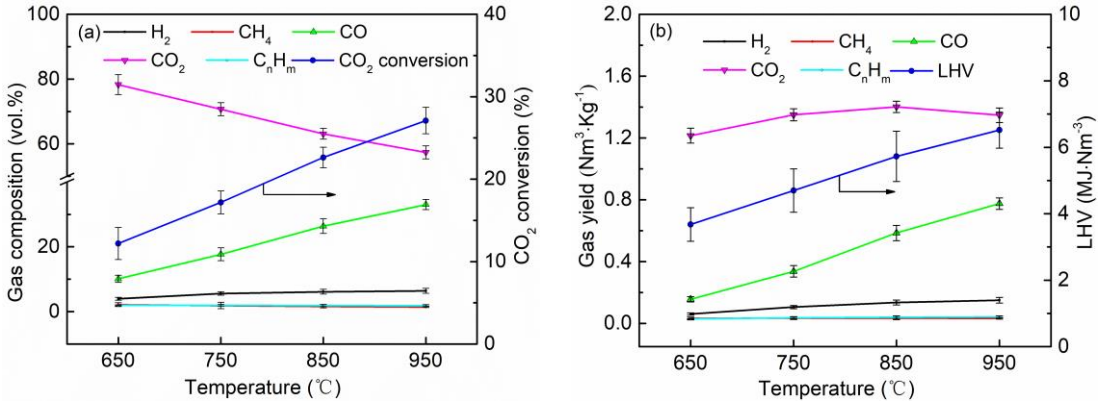

Fig. 2. Effect of temperature on the characteristics of product gas.

3.2. Physicochemical properties of biochar

3.2.1. Textural structure of biochar

The adsorption-desorption isotherms of biochar samples produced at different temperatures were illustrated in Fig. 3. According to the IUPAC classification, the adsorption isotherm of biochar samples presented the reversed S-shape between type I and type II, indicating that the pore characteristics of biochar samples were similar, continuous and complicated after the different gasification temperatures treatment. The nitrogen adsorption quantity reflects the adsorptive capacity of the biochar [32]. At extreme low pressure ($P/P_0 < 0.05$), the adsorption quantities of biochar samples at

different gasification temperatures (650 °C, 750 °C, 850 °C, and 950 °C) were 46.77 $mL \cdot g^{-1}$, 61.94 $mL \cdot g^{-1}$, 65.24 $mL \cdot g^{-1}$ and 41.15 $mL \cdot g^{-1}$, which indicated a large number of micropores. Moreover, the amount of micropores increased from 650 °C to 850 °C and decreased from 850 °C to 950 °C sharply. This revealed that the increase of gasification temperature was in favor of the formation of micropores to a certain extent because the higher temperature can not only promote the discharge of pyrolysis products but also enhance CO_2 gasification with the reactive sites. However, when the temperature rose to 950 °C, the amount of micropores in the biochar samples was the lowest. The high temperature promoted the formation of mesopores and macropores by the aggregation of original micropores during gasification. The sintering effect that can seal off the part of the micropores was another factor which should not be ignored simultaneously [32]. Fu et al. [32] found the similar trend of biochar samples that the amount of micropores increased with the increase of temperature and then decreased. Xu [41] reported that the amount of micropores increased firstly and decreased sharply due to the breaking of the microporous structure. Li et al. [42] also found the similar results that the adsorption quantity of biochar increased from 500 °C to 800 °C. However, the quantity of adsorption decreased sharply when the temperature increased from 800 °C to 900 °C.

Table 2 Textural properties of the biochar samples.

T, °C	Specific surface area, $m^2 \cdot g^{-1}$	Pore volume, $cm^3 \cdot g^{-1}$	Average pore diameter, nm	FD
650	196.68	0.12	2.46	2.9155
750	256.19	0.18	2.79	2.9118
850	277.49	0.22	3.11	2.9004
950	176.03	0.19	4.41	2.8072

As shown in Table 2, the specific surface area of the biochar samples increased from 650 °C to 850 °C and decreased from 850 °C to 950 °C. Ping et al. [43] found the variation of the specific surface area was mainly due to the formation and breaking of micropores. In the medium pressure adsorption zone ($0.05 < P/P_0 < 0.8$), the adsorption curves transformed from monolayer to multilayer adsorption and the adsorption quantities from 650 °C to 950 °C were 13.94 $mL \cdot g^{-1}$, 34.27 $mL \cdot g^{-1}$, 51.39 $mL \cdot g^{-1}$ and 46.37 $mL \cdot g^{-1}$. The adsorption quantity increased with the increase of temperature from 650 °C to 850 °C, indicating that the amount of mesopores increased. When the temperature increased from 850 °C to 950 °C, the adsorption quantity decreased showing that the amount of mesopores decreased. In the saturated pressure zone ($0.9 < P/P_0 < 0.995$), the adsorption quantities from 650 °C to 950 °C

were 17.57 mL·g^{-1}, 19.29 mL·g^{-1}, 22.90 mL·g^{-1}, and 38.02 mL·g^{-1}. The adsorption curves became steeper with the increase of temperature, indicating the capillary condensation appeared and the amount of macropores increased sharply. As the temperature increased, CO_2 reacted with the carbon skeleton, leading to the formation of macropores rapidly by the aggregation of some original mesopores. Therefore, the amount of mesopores decreased when the temperature increased from 850 °C to 950 °C. In Table 2, the pore volume increased from 650 °C to 850 °C and then decreased from 850 °C to 950 °C, while the average pore size increased from 650 °C to 950 °C. The phenomenon that two measurements had different trends showed the pore length at 950 °C was shorter than that at 850 °C, indicating that the erosion of the biochar surface through gasification in CO_2 was promoted. The variation trend of pore volume was consistent with the change in amount of micropores and mesopores. The formation and breaking of micropores and mesopores may be the reason that pore volume increased firstly and then decreased.

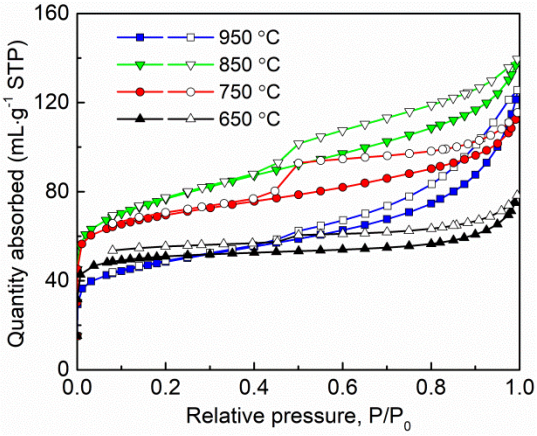

Fig. 3. Adsorption-desorption isotherm curves of the biochar samples.

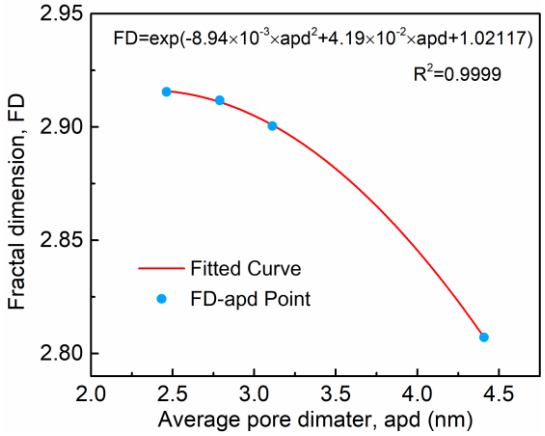

Fig. 4. Functional relationship between the average pore diameter and fractal dimension of biochar samples.

The fractal dimension values of the co-gasification biochar samples were revealed in Table 2. The values of FD decreased with the increase of gasification temperature indicating the surface roughness of biochar would decrease under the action of the gasification agent-CO_2. Curve fitting method was used to measure the functional relationship between average pore diameter and fractal dimension [32]. As shown in Fig. 4, it was clearly observed that there was an exponential relationship between the two variables as shown in the Eq. (16). The correlation coefficient R^2 was 0.9999, approximating to 1, which can well describe the relationship of the two variables reasonably. The results of fractal dimension were valid when average pore diameter ranged from 2.46 nm to 4.41 nm. The negative correlation was observed and was consistent with the results from Fu et al. [32] who found that the linear relationship between the average pore diameter and fractal dimension were based on the co-pyrolysis biochar samples. However, the above results were based on the co-gasification biochar samples. The gasification process made the evaluation of biochar more complicated and the exponential relationship can more accurately describe the two variables. As the average pore diameter increased, the FD decreased based on the function relationship providing further support for the conclusion that the sharp decrease of micropores and the increase of macropores at 950 °C promoted the growth of pore diameter and the reduction of pore length resulting in the decrease of surface roughness.

$$FD=\exp(-8.94\times10^{-3}\times apd^2+4.19\times10^{-2}\times apd+1.02117) \quad 2.46 \le apd \le 4.41 \quad (16)$$

3.2.2. FT-IR analysis of biochar

Fig. 5 showed the FT-IR spectra of the biochar samples produced at different temperatures. It was evident that there were many functional groups such as aliphatic CH_2 (1, 3000-2800 cm^{-1}), aromatic carbonyl (2, 1800-1400 cm^{-1}), ether bond (3, 1150-1085 cm^{-1}), phosphate (4, 1150-950 cm^{-1}), and aromatic CHx out of plane (5, 900-700 cm^{-1}) in the biochar [41, 44]. The absorbance intensity can be used to compare the relative content difference among the functional groups of biochar produced at different gasification temperatures. The intensity of ether bond (1091 cm^{-1}) decreased with the increase of temperature indicating that the ether bond broken at the higher temperature [41]. The largest peaks at 985 cm^{-1}, 1042 cm^{-1}, 1120 cm^{-1} belonged to the phosphates, which covered the wavenumber from 900 cm^{-1} to 1250 cm^{-1} [44-48]. As shown in Li's study, the digestate ash contained the component P_2O_5

[22]. The ash relative contents in the biochar increased with the rise of gasification temperature due to the consumption of organic matter. The reason may be that the phosphate peaks became stronger and stronger with the increasing temperature. Besides, the characteristic peaks representing the structure of aromatic C=C (1620 cm^{-1},1585 cm^{-1},1480 cm^{-1},1410 cm^{-1}) became prominent, suggesting that the aromatization trend was more and more obvious [49, 50]. The intensity of aliphatic side chains methylene (2923 cm^{-1}, 2852 cm^{-1}) decreased evidently with the increase of temperature from 650 °C to 950 °C. Methylene was the form of aliphatic side chain in the biochar, and it mainly existed in long chain. In addition, it meant that the decompose of aliphatic compounds contained in digestate and lignite were gradually completed, forming methane or other organic gas as the rise of gasification temperature [51, 52].

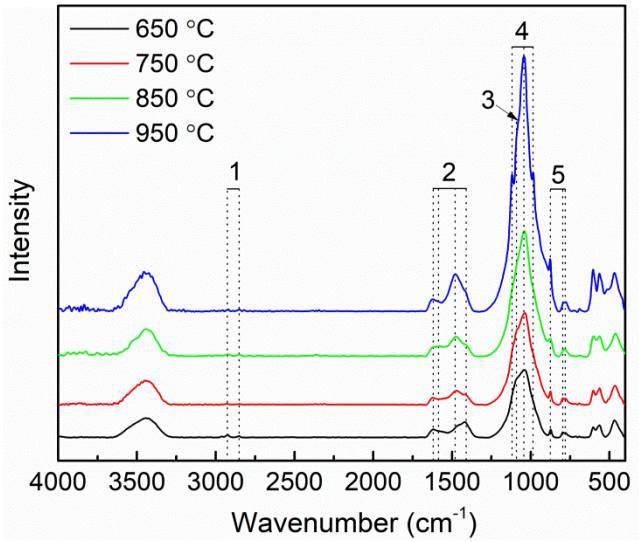

Fig. 5. FT-IR spectra of the biochar samples (1, aliphatic CH_2; 2, aromatic carbonyl; 3, ether bond; 4, phosphate; 5, aromatic CH_x out of plane).

3.2.3. Raman analysis of biochar

The Raman spectroscopy has been widely used in investigating the structural characteristics of biochar by calculating the intensity ratio among the different bands [30, 53]. Fig. 6 showed the parameters obtained from the Raman spectra of biochar produced at different temperatures. The digestate and lignite were rich in the O-containing functional groups and aliphatic structures, which were not likely to be converted into graphite structures at around 900 °C [54, 55]. The G band and D band mainly represented the aromatic ring vibration and the aromatic ring polycondensation with 6 or more polymerized aromatic rings instead of graphite and

defect structures [53, 55]. From Fig. 6a, it was clearly observed that the total peak areas decreased with the rise of gasification temperature, because the sensitive aliphatic and oxygenated groups decomposed with the increase of temperature. In addition, the increase of aromatic structure can increase the light absorptivity [53, 54, 56]. This was consistent with the FT-IR results. In Fig. 6b, the I_D/I_G, $I_D/(I_{GR}+I_{VL}+I_{VR})$ and I_S/I_G band area ratios increased when the temperature increased. The increasing I_D/I_G represented the growth in polycondensation of aromatic ring systems. The G_R, V_L and V_R bands deriving from the zone between the D band and the G band represented the smaller aromatic ring systems and the semicircle breathing of aromatic rings [44, 45, 57, 58]. The $I_D/(I_{GR}+I_{VL}+I_{VR})$ band area ratio is defined as the relative content of the large (⩾6 rings) aromatic ring systems to the small ones(3-5 fused benzene rings) [57, 58]. The increasing $I_D/(I_{GR}+I_{VL}+I_{VR})$ ratio indicated that the small aromatic rings condensed to large aromatic ring systems as the temperature rose. The S band mainly represented the $C_{aromatic}$-C_{alkyl} and C–H attached to the aromatic rings and was used to measure the substituents and crosslinking density [30, 57]. The increasing I_S/I_G band area ratio indicated the content of $C_{aromatic}$-C_{alkyl} and the crosslinking density increased with the rise of temperature [30].

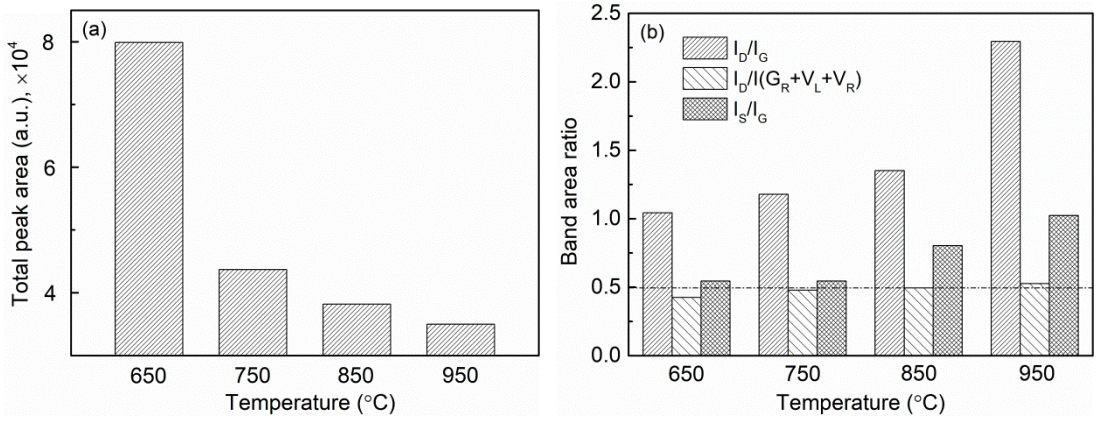

Fig. 6. Raman spectra of the biochar produced at different temperatures.

3.2.4. Reactivity of biochar in CO_2 gasification

Fig. 7 showed the gasification conversion of biochar obtained at different temperatures in CO_2. It was clearly observed that the conversion curves of biochar were quite similar. The char conversion started late at a high temperature of about 700 °C and completed around 63 min in the steam atmosphere. When the gasification was operated at higher temperature, the char conversion started much later. Hu et al. [59] investigated biochar conversion versus gasification time and found the initial

gasification temperature was around 800 °C in the steam atmosphere. As shown in Table 3, with the increase of gasification temperature from 650 °C to 950 °C, the reaction reactivities decreased slightly from 0.0154 min^{-1} to 0.0148 min^{-1}. The gasification reactivities of biochar presented the same trend that the reaction temperature affected the biochar characteristics, due to the fact that the erosion degree of biochar surface by CO_2 was different at different temperatures. According to the Section 3.2.1, a larger pore diameter was gradually formed on the surface of biochar. More highly active components escaped, thus, reducing the activity of the biochar, and higher temperatures would promote the aggregation of minerals in the mixture, resulting in the diminishing of catalysis [60, 61]. Another possible reason is that the aromatization degree of char may affect the reactivities [60, 61]. According to the Section 3.2.3, more and more small aromatic rings condensed to large aromatic ring systems as the temperature rose, the thermal stability of which was higher. The broken of large aromatic ring structure by gasification agent CO_2 needed much more energy. Therefore, the reactivities of biochar decreased when produced at higher temperature. Xu's [60, 61] study stated the same trend and concluded that there were many defects in the microcrystalline structure of char produced at low temperature, which was the active sites of gasification reaction. As the temperature increased, the number of active sites decreased and the reactivities of biochar declined.

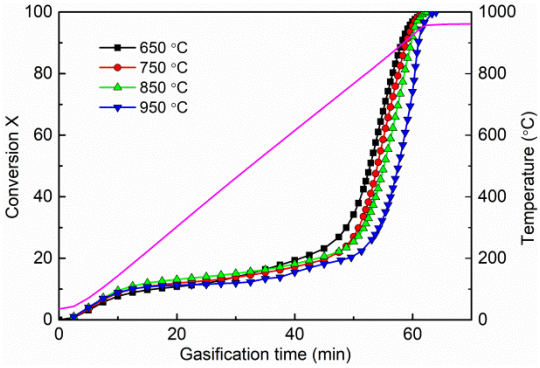

Fig. 7. Gasification conversion curves of biochar obtained from the CO_2 co-gasification.

Table 3 Gasification reactivity index of biochar.

Temperature, °C	Gasification reactivity, min^{-1}
650	0.0154
750	0.0152
850	0.0150
950	0.0148

3.3. Tar compositions

3.3.1. GC-MS

The components of tar analyzed by chromatography can be classified into the following groups: (a) alkane; (b) alkene; (c) aromatics; (d) others, with N, O and S [60]. Fig. 8 showed the effect of temperature on the tar compositions. It was noteworthy that the main composition of tar was aromatics and the contents of alkane and alkene were quite small. The content of alkane increased from 650 °C to 750 °C and decreased gradually with the rise of temperature because high temperature enhanced the hydrolysis reaction and production of alkane. In addition, the content of alkene increased because partial volatiles converted into alkene through polymerization at higher temperature. The overall trend of aromatics concentration increased with the increase of temperature. The properties of aromatics were inert and the reduction of other compounds resulted in the increase of aromatics content relatively.

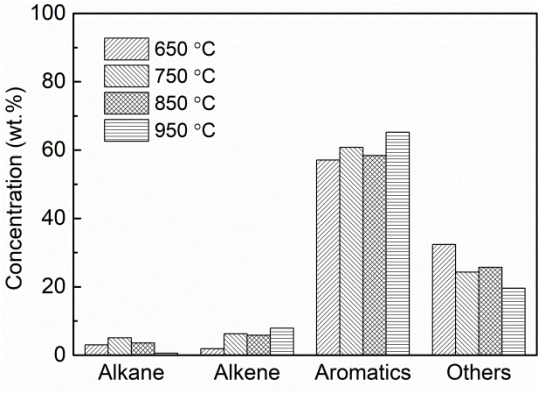

Fig. 8. Effect of temperature on the tar compositions.

Tar was the most undesirable by-product during gasification process. Tar generally appeared as a dark brown organic liquid mixture with high viscosity and low fluidity, which was poorly soluble in water. The physical properties of tar were determined by the amount of aromatics and heterocyclic compounds. The aromatics had the characteristics of high molecular weight and was easy to condense in the gasification reactor with fly ash particles, fouling and plugging pipelines of the gasification reactor. In addition, various N-heterocyclic and aromatics in the tar were toxic contaminants. If the contaminants were absorbed by the soil, surface water and groundwater, there will be a potential threat and a great challenge to the environment and human health [62].

3.3.2. Simulated distillation

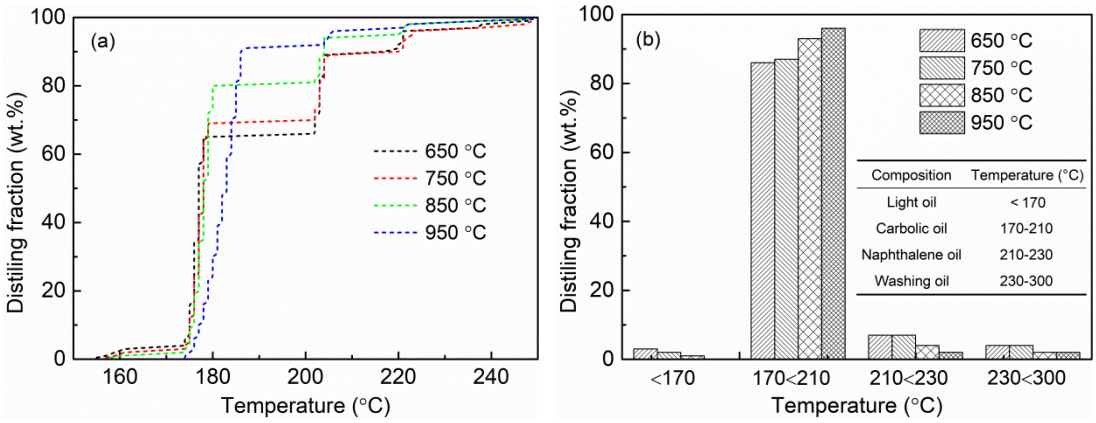

Fig. 9. Distillation fractions of tar produced from the co-gasification of digestate and lignite.

The simulated distillation can be used to analyze the fractional compositions of tar. Fig. 9 showed the distillation fractions of tar obtained from the co-gasification of digestate and lignite. In Fig. 9a, three big fractions in the tar grouped at the temperatures of 170 °C-190 °C, 200 °C-210 °C, 220 °C-250 °C. The contents of the fractions below 190 °C increased with the increase of gasification temperature, while contents of the fractions between 190 °C and 250 °C decreased evidently. It indicated that the increase of gasification temperature improved the cracking of tar, resulting in the higher yield of gas, as shown in the Section 3.1. Fig. 9b compared the contents of each distillation fraction given by the simulated distillation for the tar samples at different gasification temperatures [63]. With the increase of temperature, the content of carbolic oil increased obviously, but those of light oil, naphthalene oil and washing oil decomposed and decreased gradually. It showed that the increase of temperature promoted the secondary reaction of tar in fixed bed reactor. According to Xu' study, the similar results of the pyrolysis tar of coal showed that the heavy tar decreased and other oil contents increase slightly [60].

4. Conclusions

This study investigated the influence of temperature on co-gasification behavior of digestate and lignite in a downdraft fixed bed gasifier. The gasification temperature from 650 °C to 950 °C were tested by analyzing the characteristics of the product gas, biochar and the tar. The major conclusions of this research were summarized as below:

(1) The gasification temperature was beneficial for the increasing the gas yield

and its LHV and improving the CO_2 conversion.

(2) The effects of gasification temperature on the properties of the biochar were complicated. The increase of temperatures from 650 °C to 850 °C played a positive role in the formation of micropores. While, the sharp decrease of micropores and the formation of macropores occurred at 950 °C. Increasing the gasification temperature caused the decrease of aliphatic side chains and a growth in size and number of aromatic ring systems. Besides, as the temperature rose, the gasification reactivity became weaker gradually because of the more and more large aromatic ring systems and the less active components.

(3) With the increase of gasification temperature, the content of carbolic oil obviously increased, while the light oil, naphthalene oil and washing oil decomposed and their contents decreased gradually. The increasing temperature promoted the secondary reaction of tar in fixed-bed reactor.

Declaration of Competing Interest

The authors declare that they have no known competing financial interests or personal relationships that could have appeared to influence the work reported in this paper.

Acknowledgments

This work was supported by the National Natural Science Foundation of China (No. 21878313) and Guizhou Key Technology Support Program ([2019]2839).

References

[1] Estrada CA, Melgar A, Pérez JF. Performance prediction of a decentralized power plant (120 kWe) using a multi-particle model of a downdraft biomass gasification process. Energy Convers Manage 2019;181:258-71.

[2] Engo J. Decoupling analysis of CO_2 emissions from transport sector in Cameroon. Sustain Cities Soc 2019;51:101732.

[3] Li W, Lu C, An G, Chang S. Comparison of alkali-buffering effects and co-digestion on high-solid anaerobic digestion of horticultural waste. Energ Fuel 2017;31(10):10990-7.

[4] Barbanera M, Pelosi C, Taddeid AR, Cotana F. Optimization of bio-oil production from solid digestate by microwave assisted liquefaction. Energy Convers Manage 2018;171:1263-72.

[5] National Development and Reform Commission. National 13th five-year development plan for rural biogas. 2017. Available at: http://www.gov.cn/xinwen/2017-02/10/content_5167076.htm

[6] Cao Z, Jung D, Olszewski MP, Arauzo PJ, Kruse A. Hydrothermal carbonization of biogas digestate: Effect of digestate origin and process conditions. Waste Manage 2019;100:138-50.
[7] Chen G, Guo X, Cheng Z, Yan B, Dan Z, Ma W. Air gasification of biogas-derived digestate in a downdraft fixed bed gasifier. Waste Manage 2017;69:162-9.
[8] Li W. High-solid anaerobic codigestion of horse manure and grass in batch and semi-continuous systems. Energ Fuel 2016;30(8):6419-24.
[9] National Development and Reform Commission. The national key energy-saving low-carbon technology promotion catalogue (2017 version, low carbon section). Beijing, 2017. Available at: http://www.gov.cn/xinwen/2017-04/01/5182743/files/2bd3969838834328971fdb44a44f698d.pdf
[10] Pan ZH, Chan WP, Veksha A, Giannis A, Dou XM, Wang HM, Lisak G, Lim T. Thermodynamic analyses of synthetic natural gas production via municipal solid waste gasification, high-temperature water electrolysis and methanation. Energy Convers Manage 2019;202:112160.
[11] Balafkandeh S, Zare V, Gholamian E. Multi-objective optimization of a tri-generation system based on biomass gasification/digestion combined with S-CO2 cycle and absorption chiller. Energy Convers Manage 2019;200:112057.
[12] Rosner F, Chen Q, Rao A, Samuelsen S. Thermo-economic analyses of concepts for increasing carbon capture in high-methane syngas integrated gasification combined cycle power plants. Energy Convers Manage 2019;199:112020.
[13] Yao Z, Li W, Kan X, Dai Y, Tong, YW, Wang C. Anaerobic digestion and gasification hybrid system for potential energy recovery from yard waste and woody biomass. Energy 2017;124:133-45.
[14] Hu M, Gao L, Chen Z, Ma C, Zhou Y, Chen J, Ma S, Laghari M, Xiao B, Zhang B, Guo D. Syngas production by catalytic in-situ steam co-gasification of wet sewage sludge and pine sawdust. Energy Convers Manage 2016;111:409-16.
[15] Xu T, Bhattacharya S. Direct and two-step gasification behaviour of Victorian brown coals in an entrained flow reactor. Energy Convers Manage 2019;195:1044-55.
[16] Wang Y, Tang Y, Guo X, Xie Q, Finkelman RB, Li P, Chen P. Fate of potentially hazardous trace elements during the entrained-flow coal gasification processes in China. Sci Total Environ 2019;668:854-66.
[17] BP. BP energy outlook. Country insight-China; 2018.
[18] Nsaful F, Görgens JF, Knoetze JH. Comparison of combustion and pyrolysis for energy generation in a sugarcane mill. Energy Convers Manage 2013;74:524-34.
[19] Jayaraman K, Gökalp I. Pyrolysis, combustion and gasification characteristics of miscanthus and sewage sludge. Energy Convers Manage 2015;89:83-91.
[20] Thengane SK, Gupta A, Mahajani SM. Co-gasification of high ash biomass and high ash coal in downdraft gasifier. Bioresour Technol 2019;273:159-68.
[21] Wu Z, Meng H, Luo Z, Chen L, Zhao J, Wang S. Performance evaluation on co-gasification of bituminous coal and wheat straw in entrained flow gasification system. Int J Hydrogen Energ 2017;42(30):18884-93.
[22] Chang S, Zhang Z, Cao L, Ma L, Wang F, Li J, Li W. Interaction and kinetics study of the co-gasification of high-solid anaerobic digestate and lignite. Molecules 2020;25:459.
[23] Hayashi J, Kudo S, Kim H, Norinaga K, Matsuoka K, Hosokai S. Low-temperature gasification of biomass and lignite: consideration of key thermochemical phenomena, rearrangement of reactions, and reactor

612 configuration. Energ Fuel 2014;28:4-21.
613 [24] Cortazar M, Alvarez J, Lopez G, Amutio M, Santamaria L, Bilbao J, Olazar M.
614 Role of temperature on gasification performance and tar composition in a fountain
615 enhanced conical spouted bed reactor. Energy Convers Manage
616 2018;171:1589-97.
617 [25] Widjaya ER, Chen G, Bowtell L, Hills C. Gasification of non-woody biomass: A
618 literature review. Renew Sust Energ Rev 2018;89:184-93.
619 [26] Collot AG, Zhuo Y, Dugwell DR, Kandiyoti R. Co-pyrolysis and co-gasification of
620 coal and biomass in bench-scale fixed-bed and fluidised bed reactors. Fuel
621 1999;78(6):667-79.
622 [27] Lv P, Xiong Z, Chang J, Wu C, Chen Y, Zhu J. An experimental study on biomass
623 air–steam gasification in a fluidized bed. Bioresour Technol 2004;95:95-101.
624 [28] Zhang D. Study on co-pyrolysis and gasification characteristics of distillers' grains
625 and coal. Master thesis. Guizhou University. Guiyang. 2016.
626 [29] Pio D, Tarelho L, Tavares A, Matos M, Silva V. Co-gasification of refused
627 derived fuel and biomass in a pilot-scale bubbling fluidized bed reactor. Energy
628 Convers Manage 2020;206:112476.
629 [30] Li X, Hayashi J, Li C. FT-Raman spectroscopic study of the evolution of char
630 structure during the pyrolysis of a Victorian brown coal. Fuel
631 2006;85(12):1700-07.
632 [31] Mosqueda A, Wei J, Medrano K, Gonzales H, Ding L, Yu G, Yoshikawa K.
633 Co-gasification reactivity and synergy of banana residue hydrochar and anthracite
634 coal blends. Appl Energy 2019;250:92-7.
635 [32] Fu P, Hu S, Xiang J, Sun L, Su S, Wang J. Evaluation of the porous structure
636 development of chars from pyrolysis of rice straw: Effects of pyrolysis
637 temperature and heating rate. J Anal Appl Pyrol 2012;98:177-83.
638 [33] Avnir D, Jaroniec, M. An isotherm equation for adsorption on fractal surfaces of
639 heterogeneous porous materials. Langmuir 1989;5(6):1431-3.
640 [34] Jaroniec M. Evaluation of the fractal dimension from a single adsorption-isotherm.
641 Langmuir 1995;11(6):2316-17.
642 [35] Wang Z, Burra K G, Lei T, Gupta A. Co-gasification characteristics of waste tire
643 and pine bark mixtures in CO2 atmosphere. Fuel 2019;257:116025.
644 [36] Saha P, Helal U, Toufiq R. A steady-state equilibrium-based carbon dioxide
645 gasification simulation model for hydrothermally carbonized cow manure. Energy
646 Convers Manage 2019;191:12-22.
647 [37] Cantelo R. The thermal decomposition of methane. J Chem Phys
648 1924;28:1036-48.
649 [38] Xu C, Hu S, Xiang J, Zhang L, Sun L, Shuai C, Chen Q, He L, Edreis EMA.
650 Interaction and kinetic analysis for coal and biomass co-gasification by TG–FTIR.
651 Bioresour Technol 2014;154:313-21.s
652 [39] Kan X, Chen XP, Shen Y, Alexei A L, Kraft M, Wang C H. Box-Behnken design
653 based CO2 co-gasification of horticultural waste and sewage sludge with
654 addition of ash from waste as catalyst, Appl Energ 2019;242:1549–1561.
655 [40] You SM, Wang W, Dai YJ, Tong YW, Wang CH. Comparison of the
656 co-gasification of sewage sludge and food wastes and cost-benefit analysis of
657 gasification- and incineration-based waste treatment schemes. Bioresour Technol
658 2016;218:595-605.
659 [41] Xu C. Study on reaction mechanism and its performance of coal and biomass
660 co-gasification with steam. Doctoral Thesis. Huazhong University of science and
661 technology. Wuhan. 2014.

[42] Li W, Wu S, Wu Y, Huang S, Gao J. Gasification characteristics of biomass at a high-temperature steam atmosphere. Fuel Process Technol 2019;194:106090.
[43] Ping C, Zhou J, Cheng J, Yang W, Cen K. Surface structure of blended coals during pyrolysis (in Chinese). J Chem Ind Eng (China) 2007;58(7):1793-9.
[44] Lu Y, Deng Z. Practical infrared spectrum analysis (in Chinese). Beijing, 1989.
[45] Antonov EN, Bagratashvili VN, Popov VK, Sobol EN, Howdle SM. Determination of the stability of laser deposited apatite coatings in phosphate buffered saline solution using Fourier transform infrared (FTIR) spectroscopy. Spectrochim Acta A 1996;52(1):123-7.
[46] Lim SC, Vaughey JT, Harrison WTA, Dussack LL, Jacobson AJ, Johnson JW. Redox transformations of simple vanadium phosphates: the synthesis of ϵ-$VOPO_4$. Solid State Ionics 1996;84(3):219-26.
[47] Viala S, Freche M, Lacout JL. Effect of chitosan on octacalcium phosphate crystal growth. Carbohyd Polym 1996;29(3):197-201.
[48] Shanghai Institute of Organic Chemistry of CAS. Chemistry Database. Available at: http://www.organchem.csdb.cn.[1978-2019]
[49] Chen Y, Yang H, Wang X, Zhang S, Chen H. Biomass-based pyrolytic polygeneration system on cotton stalk pyrolysis: Influence of temperature. Bioresour Technol 2012;107:411-8.
[50] Xu M, Wu Y, Nan D, Lu Q, Yang Y. Effects of gaseous agents on the evolution of char physical and chemical structures during biomass gasification. Bioresour Technol 2019;292:121994.
[51] Hu J, Chen Y, Qian K, Yang Z, Yang H, Li Y, Chen H. Evolution of char structure during mengdong coal pyrolysis: Influence of temperature and K_2CO_3. Fuel Process Technol 2017;159:178-86.
[52] Zhang K, Li Y, Wang Z, Li Q, Whiddon R, He Y, Cen K. Pyrolysis behavior of a typical Chinese sub-bituminous Zhundong coal from moderate to high temperatures. Fuel 2016;185:701-8.
[53] Asadullah M, Zhang S, Min Z, Yimsiri P, Li C. Effects of biomass char structure on its gasification reactivity. Bioresour Technol 2010;101 (20):7935-43.
[54] Guo X, Tay HL, Zhang S, Li C. Changes in char structure during the gasification of a victorian brown coal in steam and oxygen at 800 °C. Energ Fuel 2008;22(6):4034-8.
[55] Yu J, Sun L, Berrueco C, Fidalgo B, Paterson N, Millan M. Influence of temperature and particle size on structural characteristics of chars from Beechwood pyrolysis. J Anal Appl Pyrol 2018;130:127-34.
[56] Ito O. Diffuse reflectance spectra of coals in the UV-visible and near-IR regions. Energ Fuel 1992;6(5):662-5.
[57] Li C. Some recent advances in the understanding of the pyrolysis and gasification behaviour of Victorian brown coal. Fuel 2007;86(12):1664-83.
[58] Lin D, Liu L, Zhao Y, Zhaso Y, Qiu P, Xie X, Sun S. Physicochemical structure characteristics and intrinsic reactivity of demineralized coal char rapidly pyrolyzed at elevated pressure. J Energy Inst 2019. In press.
[59] Hu J, Shao J, Yang H, Lin G, Chen Y, Wang X, Zhang W, Chen H. Co-gasification of coal and biomass: Synergy, characterization and reactivity of the residual char. Bioresour Technol 2017;244:1-7.
[60] Xu S, Zeng X, Han Z, Cheng J, Wu R, Chen Z, Masěk O, Fan X, Xu G. Quick pyrolysis of a massive coal sample via rapid infrared heating. Appl Energy 2019;242:732-40.
[61] Xu S. Coal pyrolysis for oil and gas with infarared quick heating and staged

712 reaction control. Doctoral thesis. Chinese Academy of Sciences. Beijing. 2019.
713 [62] Guo F, Jia X, Liang S, Zhou N, Chen P, Ruan R. Catalytic cracking of biomass
714 pyrolysis tar over char-supported catalysts. Energy Convers Manage
715 2018;167:81-90.
716 [63] Zeng X, Wang F, Li H, et al. Pilot verification of a low-tar two-stage coal
717 gasification process with a fluidized bed pyrolyzer and fixed bed gasifier. Appl
718 Energy 2014;115:9-16.